PERGAMON

Acta mater. Vol. 47, No. 7, pp. 2089–2108, 1999

Printed in Great Britain
PII: S1359-6454(99)00083-X
1359-6454/99 $20.00 + 0.00

SHOCK CONSOLIDATION: MICROSTRUCTURALLY-BASED ANALYSIS AND COMPUTATIONAL MODELING

M. A. MEYERS[1], D. J. BENSON[1] and E. A. OLEVSKY[2]†

[1]Department of Applied Mechanics and Engineering Sciences, University of California, San Diego, La Jolla, CA 92093-0411, U.S.A. and [2]Department of Mechanical Engineering, College of Engineering, San Diego State University, San Diego, CA 92182-1323, U.S.A.

(Received 12 October 1998; accepted 4 March 1999)

Abstract—The most important microstructural processes involved in shock consolidation are identified and discussed; the energy dissipated by a shock wave as it traverses a powder is assessed. The basic microstructural phenomena are illustrated for a metal (nickel-based superalloy), an intermetallic compound (rapidly solidified Ti_3Al), and ceramics (silicon carbide). Interparticle melting, vorticity, voids, and particle fracture are observed and the plastic deformation patterns are identified. Various energy dissipation processes are estimated: plastic deformation, interparticle friction, microkinetic energy, and defect generation. An analytical expression is developed for the energy requirement to shock consolidate a powder as a function of strength, size, porosity, and temperature, based on a prescribed interparticle melting layer. This formulation enables the prediction of pressures required to shock consolidate materials; results of calculations for the superalloy and silicon carbide as a function of particle size and porosity are represented. The fracture of ceramic particles under shock compression is discussed. Tensile stresses are generated during compaction that may lead to fracture. It is shown that the activation of flaws occurs at tensile reflected pulses that are a decreasing fraction of the compressive pulse, as the powder strength increases. These analytical results are compared to numerical solutions obtained by modeling the compaction of a discrete set of particles with an Eulerian finite element program. These results confirm the increasing difficulty encountered in shock consolidating harder materials, and point out three possible solutions: (a) reduction of initial particle size; (b) reduction of shock energy; (c) post-shock thermal treatment. Two possible and potentially fruitful approaches are to shock densify (collapse voids with minimum bonding) powders and to apply post-shock thermal treatments, and to shock consolidate nanosized powders. The latter method requires high shock energy and careful minimization of the shock reflections.

1. INTRODUCTION

Shock consolidation has been an intensively investigated method since the 1980s [1]. It is very important to estimate the total energy needed to consolidate a material and to determine the shock parameters required to effect such a consolidation by shock waves. This predictive capability has been obtained, for soft materials, through the energy flux models of Gourdin [2] and Schwarz *et al.* [3]. Raybould *et al.* [4] also presented a planar and one-dimensional approach which is based on the shock rise time and thermal conduction equilibrium. For harder materials, the energy expended in plastic deformation becomes an important component of the overall energy balance equation. Energy predictions incorporating plastic work have been made by Nesterenko [5], Ferreira and Meyers [6], and Ahrens *et al.* [7]. Comprehensive recent treatments by Sawaoka [8] and Horie and Sawaoka [9] are noteworthy. Various shock-compaction mechanisms have been discussed by Kondo and co-workers [10, 11].

Recently, large-scale Eulerian computations using a two-dimensional geometry (cylindrical particles) have been used to model shock consolidation. The calculation procedure developed by Benson and Nellis [12] is an extension of the work of Williamson [13] and uses an Eulerian finite element code well suited for the description of large plastic deformations occurring in shock consolidation.

The identification and quantitative evaluation of the various phenomena occurring during the propagation of a shock wave through a powder is a necessary step in the estimation of the overall energy requirements. Figure 1 shows these phenomena schematically. These are: (a) *Plastic deformation energy*: The material is plastically deformed; the collapse of the voids requires plastic flow. A plastic deformation energy has to be computed. (b) *Microkinetic energy*: The plastic flow of the material is a dynamic process, leading to an interparticle impact, friction, and plastic flow beyond the flow geometrically necessary to collapse the voids. This component is called "microkinetic energy" [5]. Examples of intense energy deposition with localized heating as a result of the kinetic energy of the

†To whom all correspondence should be addressed.

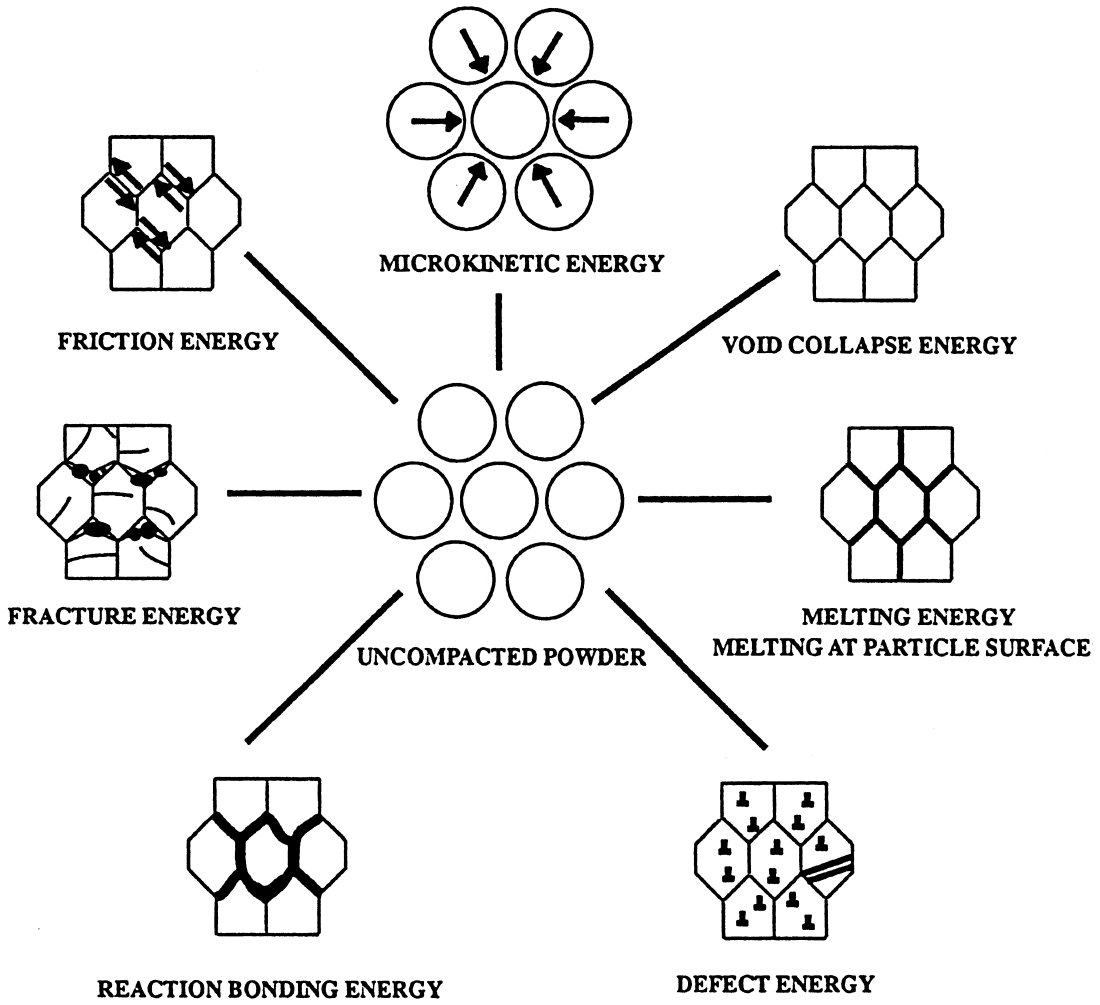

Fig. 1. Various modes of energy dissipation in shock compression of powders.

system are the formation of a jet at the interface between two plates in explosive welding and the temperature rise in the formation of shaped charge jets. The entire plastic deformation path is changed by virtue of the dynamics of the process. The kinetic energy acquired by the material elements being plastically deformed eventually dissipates into thermal energy. (c) *Melting at interparticle regions*: It is known that energy is preferentially deposited at the particle surface, leading eventually to their melting. This is the main component of the model suggested by Schwarz *et al.* [3]. (d) *Defect energy*: Point, line, and interfacial defects are produced by the passage of the shock wave. Meyers and Murr [14] have provided quantitative assessments of these defect concentrations in shock-wave deformation. (e) *Friction energy*: The rearrangement of the powders at the shock front requires relative motions, under the four applied stresses. Thus, friction may play a role in energy deposition at the shock front. (f) *Fracture energy*: Brittle materials may consolidate by fracturing. The comminuted particles can more efficiently fill the voids. (g) *Gas compression*: Compaction is most often conducted with the powder being initially at atmospheric pressure. Thus, the gaps between the powders are filled with gas. Shock compaction of the powders compresses and heats these gases. This effect was considered first by Lotrich *et al.* [15]. Elliott and Staudhammer [16] demonstrated, by conducting compaction experiments at different gas pressures, the importance of the interparticle gas influence on shock consolidation. (h) *Shock initiated chemical reactions*: Reactive elements or compounds can be added to the powders that are being consolidated. These exothermic reactions can be used to deposit additional energy at the powder surfaces, thereby assisting bonding. This approach was introduced by Akashi and Sawaoka [17] and was extended to intermetallic compounds by Shang and Meyers [18].

The eight "components" of the processes occurring during the passage of a shock wave through a granular medium described above and presented schematically in Fig. 1 are not independent and there is some overlap. This is not a rigorous classification and should only be considered as a simplified

explanation. For instance, microkinetic energy (b) and plastic deformation energy (a) contribute to melting at the interparticle regions (c). On the other hand, fracture energy (f) and plastic deformation energy (a) are competing processes and densification can occur by either one or a combination of both processes.

The schematic diagram of Fig. 1 will be illustrated in Section 2 through specific examples. In Section 3, a simple "engineering" model is presented, incorporating the principal phenomena shown in Fig. 1; this model enables predictions of the pressures required for powder consolidation as a function of particle strength, particle size, and porosity. Section 4 presents results of large-scale computations in which the principal features discussed in Sections 1–3 are predicted by modeling. Inconel 718 and silicon carbide are chosen as model metal and ceramic materials, respectively, in the metallographic observations (Section 2), analytical calculations (Section 3), and computational modeling (Section 4). In Section 5 limitations of shock-consolidation processes, such as particle damage, are discussed.

2. MICROSTRUCTURAL CHARACTERISTICS OF SHOCK-CONSOLIDATED MATERIAL

2.1. Observation in shock-consolidated materials

The essential features of shock-consolidated materials are reviewed in order to be compared to the predictions of Sections 3 and 4. The impact between particles, in metals, does not lead to symmetric plastic deformation that would be predicted from a hydrostatic, quasistatic compression when the particle velocity is below a few hundreds of meters per second.

The formation of jets, and the deformation of spherical particles into "parachutes" is shown by arrows A in Fig. 2 (shock-consolidated Inconel 718 superalloy). The tips of these regions, in Fig. 2, show evidence of melting (arrows B). The white areas formed from the dendrite structure of the particles are due to interparticle melting. The same phenomenon is observed in Fig. 3 for Ti_3Al [melting is shown by arrow A in Fig. 3(a)]. These clear regions are microcrystalline or nanocrystalline in structure, as illustrated by Fig. 4, which shows grains with an approximate diameter of 0.1 μm and the corresponding diffraction pattern for Inconel 718. Evidence for vorticity, or redundant plastic deformation, is also presented in Figs 2 and 3, and is marked by arrows C. Important additional features shown in Figs 2(b) and 3(b) are voids (marked by arrows D) which are produced by the shrinking associated with solidification of the interparticle melt regions. This is also demonstrated in Fig. 5. As shown by Wang *et al.* [19], these voids contribute to the embrittlement of the shock-consolidated material because they are initiation sites for cracks during deformation. Vorticity leading to material being propelled into the void regions due to the high kinetic energy is clearly seen in Fig. 6(a); the material is a rapidly solidified Ti_3Al intermetallic-based compound that was shock consolidated by Ferreira and Meyers [6]. The white regions represent melted and resolidified material. "Parachute" shaped particles are again seen, and are marked by B. Inhomogeneous deformation in the form of small regions of shear localization (arrow C) is shown in Figs 6(a) and (b).

The behavior of shock-consolidated ceramics can be quite different. Although it is well known that ceramic particles can undergo plastic deformation in shock consolidation and that interparticle melting contributes to bonding, there are reports of particle fracture and bonding without interparticle melting. Transmission electron microscopy inevitably reveals a high density of defects in shock-processed ceramics. The interparticle melt regions are smaller than in the case of metals and it is even possible that these layers are often overlooked. Figure 7 shows the interface between three particles in shock-consolidated SiC. The clear region has a width of 1 μm, and spheroidal particles with a diameter of 1–20 nm are seen. These are crystallization centers inside an amorphous region. The cooling rate was so high that crystallization of the molten interparticle SiC layer was almost completely inhibited.

Thus, melting and resolidification may play a role in ceramic shock consolidation. A second and very important feature of shock-consolidated ceramics is shown in Fig. 8. Often, particles fracture under the effect of shock waves. The stresses set up within the particles are highly inhomogeneous, and existing flaws can be activated by tensile stresses due to, for instance, bending of the particles. It has been observed that larger particles tend to fracture whereas small particles preferentially undergo plastic deformation. This phenomenon is analyzed in Section 5.1.

2.2. Model experiment

An important question, that has a fundamental bearing on the mechanical performance of shock-consolidated materials, is: what fraction of the surface of a particle is bonded to its neighbors? It is easy to realize that the molten regions are not uniformly distributed between the particles, and that a continuous layer of interparticle melted material would require a significant fraction of melting of the compact (30–40%). The existence of discrete and discontinuous melting/bonding regions would ensure integrity to the compact; however, the mechanical strength would be severely reduced. In order to determine to what extent the particles bond, a large-scale experiment was carried out (Fig. 9). Ideally, it should involve two spheres [Fig. 9(a)],

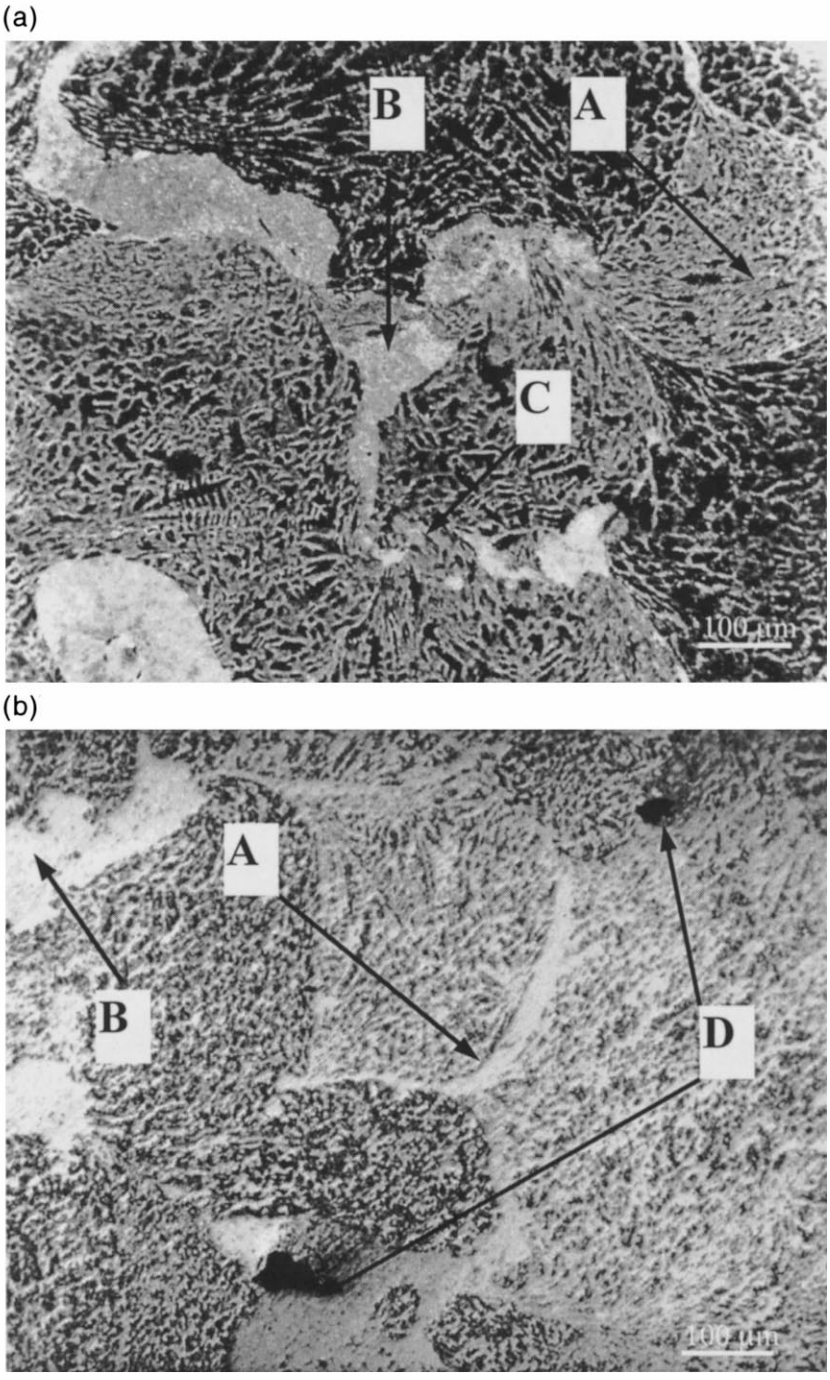

Fig. 2. Optical micrographs of shock-consolidated Inconel 718 powder showing molten and resolidified regions (B); particles deformed into a "parachute" shape (A); evidence of vorticity and voids (D).

but it was not possible to successfully carry out this experiment: the spheres fractured. A flat plate (Al) was therefore propelled against a semi-cylinder (Cu) [Fig. 9(b)]. The differences between regions A and B are striking. Region A corresponds to normal impact, whereas region B corresponds to inclined impact. Normal impact does not yield any bonding [Fig. 10(a)]; inclined impact leads to severe interfacial deformation and bonding [Fig. 10(b)]. The dark interfacial layer in Fig. 10(a) is surface oxide, which is intact, whereas it is removed by interfacial friction, jetting, and extended plastic deformation in Fig. 10(b). These results indicate clearly that interparticle bonding, as shown in a schematic fashion in Fig. 9(a), is highly inhomogeneous. The regions of the particles that are in contact with each other show rather deficient bonding; on the other hand, the regions interfacing interparticle voids undergo

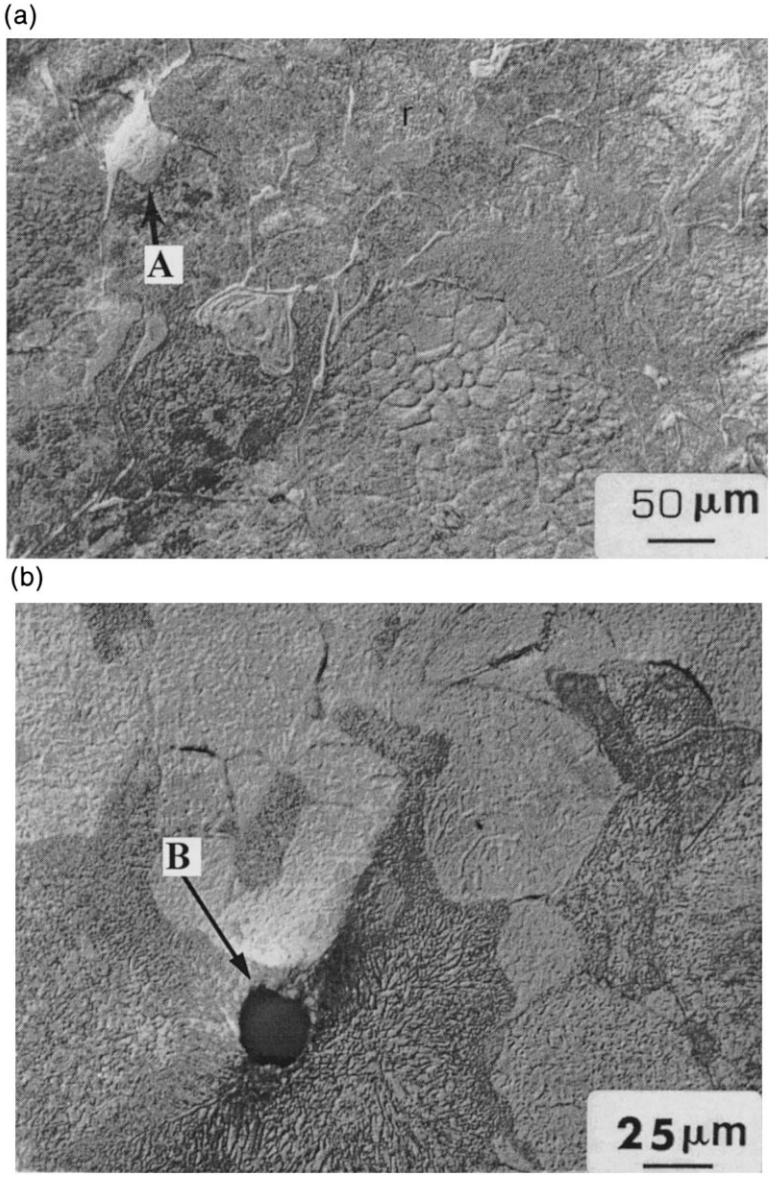

Fig. 3. Optical micrographs of shock-consolidated Ti_3Al showing evidence of melted and rapidly solidified material (A) and shrinkage void at the center of melting pool (B).

extensive plastic deformation, friction, and melting, and therefore bond. This phenomenon is modeled in Section 4.

3. ANALYTICAL CALCULATION OF ENERGY REQUIREMENTS FOR SHOCK COMPACTION

3.1. Void collapse energy at microscopic level

The void collapse energy is strongly affected by particle geometry, particle contact areas and mechanical properties of the particle and adjacent particle. One of the models that predict the pressure in porous materials as a function of density is that by Helle *et al.* [20] (a review of the related models of densification has been recently published by Olevsky [21]). The interparticle pressure, P_{int}, was found to be related to the effective applied pressure, P_{eff}, by

$$P_{\text{int}} = \frac{P_{\text{eff}}(1-\rho_0)}{\rho^2(\rho-\rho_0)} \tag{1}$$

where P_{eff} and ρ are the applied stress and current relative density, respectively; ρ_0 is the initial relative density. The plastic yield condition [22, 23] is assumed to be

$$P_{\text{int}} \geq 2.97\, Y_{\text{y}}. \tag{2}$$

where Y_{y} is the flow stress of the material. The effective yield stress is given by

$$P_{\text{y}} = 2.97\rho^2 \frac{(\rho-\rho_0)}{(1-\rho_0)}\, Y_{\text{y}}. \tag{3}$$

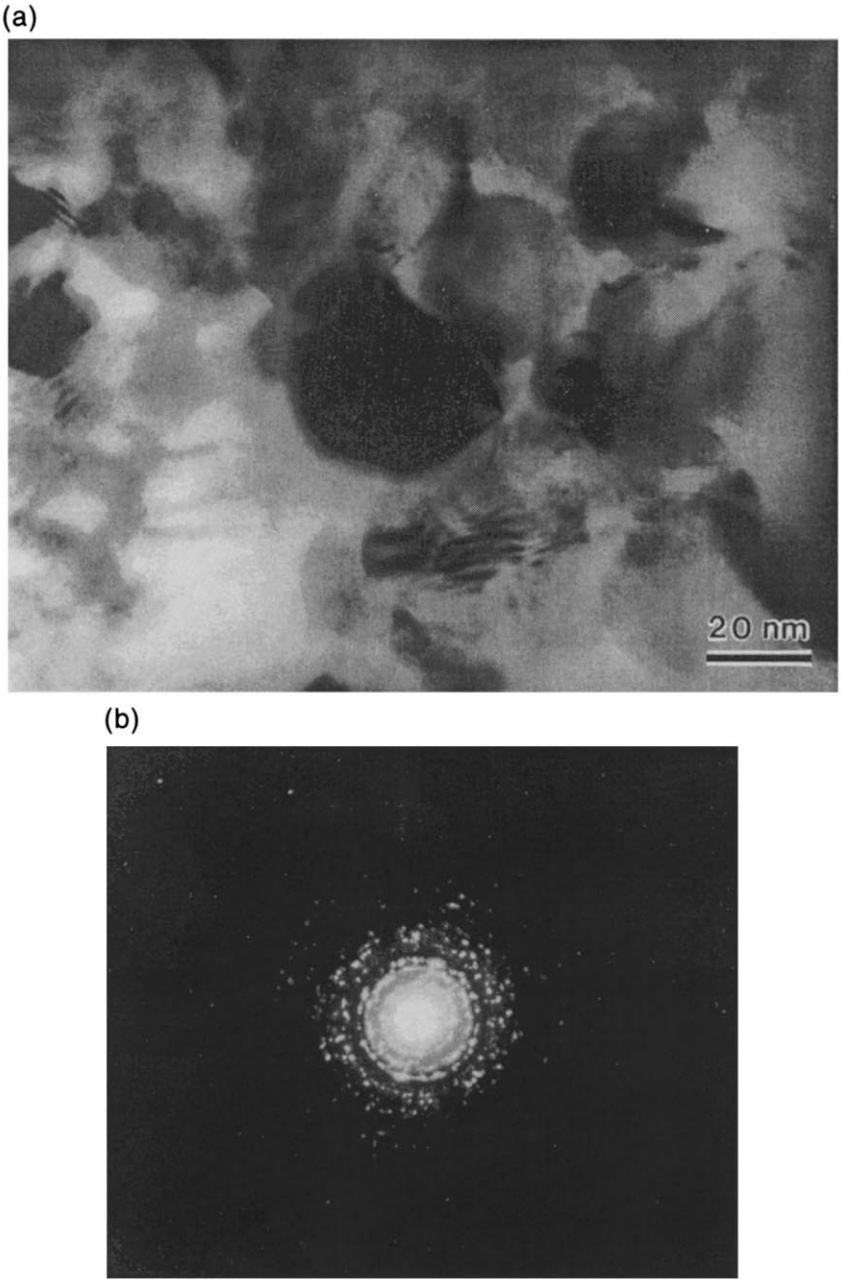

Fig. 4. (a) Transmission electron micrograph of molten/resolidified region in shock-consolidated Inconel 718 powder. (b) Electron diffraction pattern.

The specific energy (per unit volume of the substance) required to densify the material is given by

$$E_{\mathrm{vc}} = -\int_{\rho_0}^{\rho} P_{\mathrm{y}} \frac{1}{\rho^2} \mathrm{d}\rho$$

or

$$E_{\mathrm{vc}} = \frac{2.97 Y_{\mathrm{y}}}{1-\rho_0}\left[\rho\rho_0 - \frac{(\rho^2+\rho_0^2)}{2}\right]. \qquad (4)$$

Another commonly used constitutive model is the Carroll–Holt model. The comparison between the calculated pressures as a function of density for both models is shown in Fig. 11. The Helle *et al.* model [20] represents both the initial and intermediate stages of consolidation (up to $\rho = 0.92$), whereas the Carroll–Holt model represents more effectively the collapse of isolated spherical pores (the last stages, from $\rho = 0.92$ to 1).

3.2. Microkinetic energy

Nesterenko [5] developed a model which describes the relative movement of particles under dynamic compression, as shown in Fig. 12. This is a modifi-

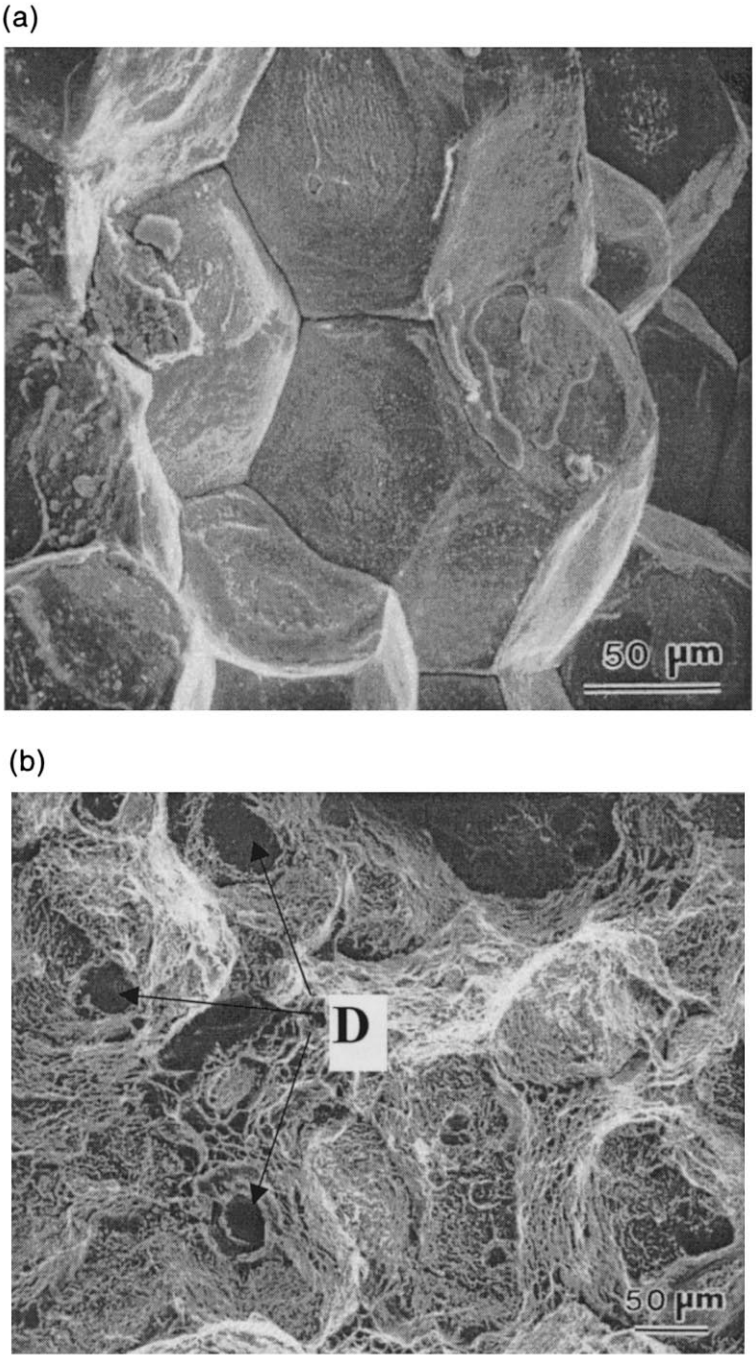

Fig. 5. SEM micrographs of shock-consolidated Ti_3Al powder: (a) shock energy is low, insufficient for melting in interparticle areas; (b) shock energy is sufficient for melting of interparticle areas; evidence of voids (D) produced by the shrinking associated with solidification of the interparticle melt regions.

cation of the Carroll–Holt model [24] which considers the porous material as a hollow sphere, which is pressurized from the outside and, as a consequence, undergoes plastic deformation with a decrease in the internal radius. Nesterenko's [5] modification of the Carroll–Holt model enables the introduction of a size scale and the separation of the plastic deformation process into two components, one of which has a substantial microkinetic energy. The external shell, with a mass m, is directly responsible for the microkinetic energy, since it impacts the internal core, which is considered to be stationary. In this model, the external shell impacts the central core (with radius c) at an

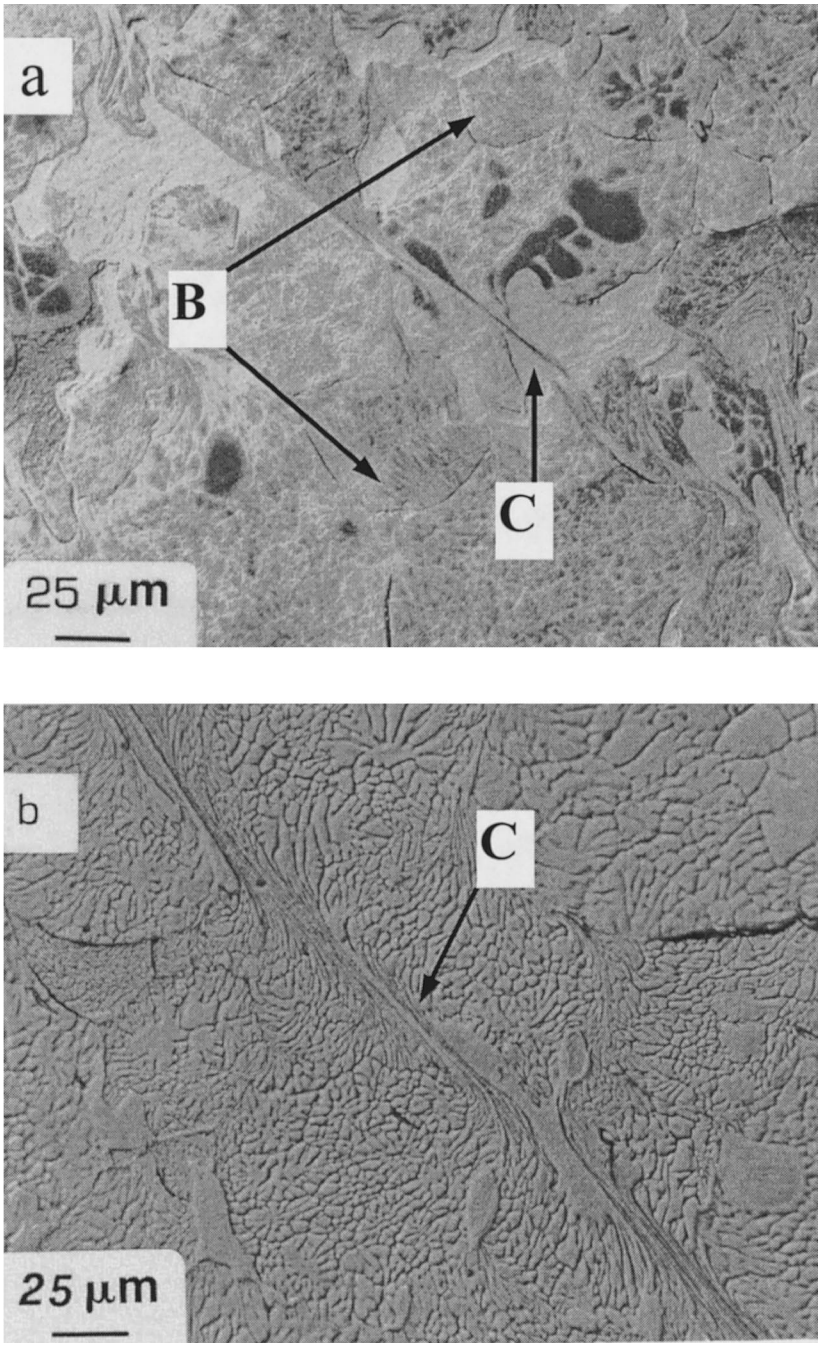

Fig. 6. Optical micrographs showing localized shear deformation (C) and interparticle melting (B) along the shear zone in Ti_3Al alloy compact.

impact velocity of V. This impact velocity is estimated to be

$$V = \frac{\text{average relative movement of particles}}{\text{shock rise time}}. \quad (5)$$

The interstitial void volume is dependent on particle size. Relative movement of particles, upon densification, is greater for large particle size, causing larger deformation per interstitial site. The dimensions of the central core and shell are defined as: $a_0 = D$; $c = D(2 - \alpha_0)^{1/3}$ where α_0 is the initial distention ($\alpha = 1/\rho$); and D is the average particle size. The shock rise time, τ, can be estimated from transit time through one particle. The impact velocity is given by $V = (a_0 - c)/\tau$, and the specific microkinetic energy (per unit volume) is given as

$$E_k = \frac{1}{2}mV^2 = \frac{1}{2}m\left(\frac{a_0 - c}{\tau}\right)^2 \quad (6)$$

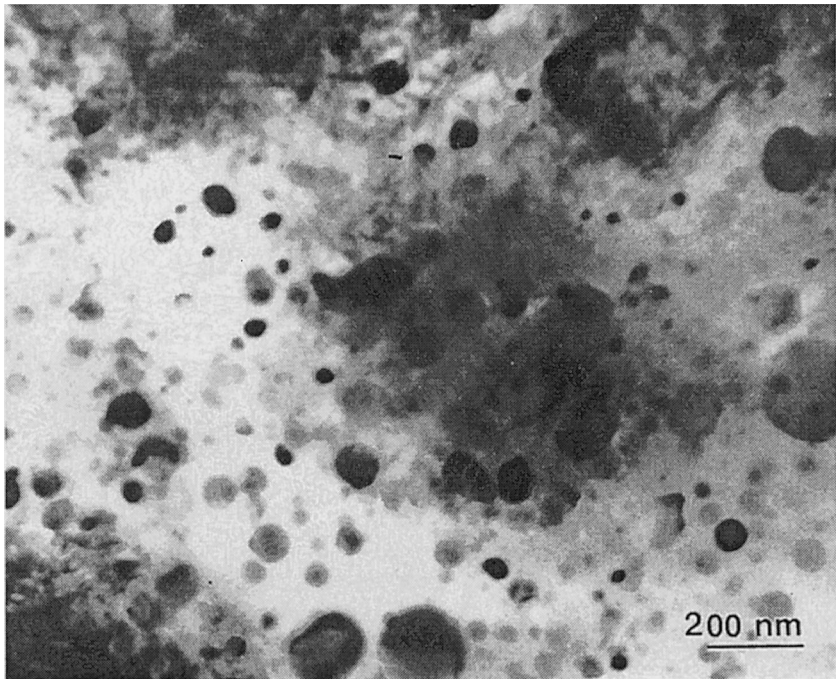

Fig. 7. Transmission electron micrograph of shock-consolidated 44 μm SiC showing amorphous interparticle region in which small crystal nucleates.

where m is the volumetric mass of the external shell:

$$m = \frac{b_0^3 - a_0^3}{b_0^3 - a_0^3 + c^3}\rho_T \tag{7}$$

where ρ_T is the theoretical density of the material. Eulerian finite element calculations by Benson *et al.* [30] enabled the quantitative estimation of the microkinetic energy.

3.3. Defect energy

Shock energy is also deposited into the interiors of the particles by generating high dislocation densities and deformation twinning. This energy stored in the elastic strain fields of dislocations can be estimated from the specific energy of a dislocation line (per unit volume) [25]:

$$E_d = \left(\frac{Gb^2}{10} + \frac{Gb^2}{4\pi}\ln\frac{\rho_d^{-1/2}}{5b}\right)\rho \tag{8}$$

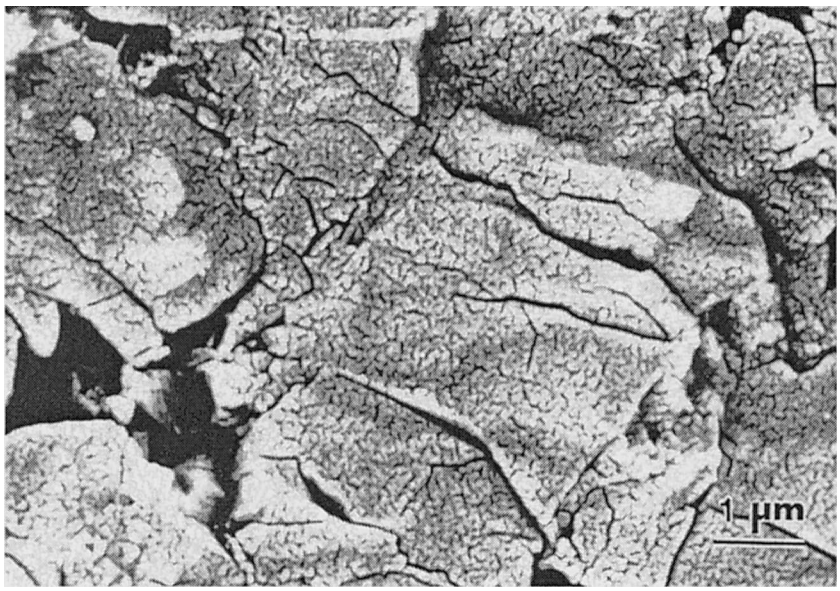

Fig. 8. Particle fracture produced by shock consolidation of silicon carbide (initial particle size equal to 7 μm).

where G is the shear modulus, b the Burgers vector, and ρ_d the dislocation density. At high shock pressures, the dislocations are usually too dense to allow quantification of the dislocation density. The practical limit for measurable dislocation density is about 5×10^{11} cm^2. The defect energy per unit mass E_d/ρ_0 (ρ_0 is the initial density of the particle) has been calculated and is found to be between 1 and 15 kJ/kg. This is a part of the deformation energy and is incorporated into the void collapse energy.

3.4. Melting energy

It has been shown that the melt fraction depends on shock pressure, void volume, void size distribution, and particle strain. The specific melting energy (per unit volume) can be expressed in the following form:

$$E_m = L[\bar{C}_p(T_m - T_0) + H_m] \tag{9}$$

where L is the volume fraction melted, $\bar{C}_p$ the average value of specific heat per unit volume, T_m the melting temperature, T_0 the initial temperature of the powder, and H_m the latent heat of melting per unit volume.

3.5. Frictional energy

The calculation of frictional energy is based on a pyramidal coordination and one-dimensional strain. Four uniform solid spheres occupy the four corners of a pyramid, as shown in Fig. 13.

The volume of a pyramidal unit cell is

$$V_0 = 1/3hA = \frac{\sqrt{2}}{12}D^3 \tag{10}$$

where

$$h = \frac{\sqrt{2}}{\sqrt{3}}D, \; A = \frac{\sqrt{3}}{4}D^2 \tag{11}$$

h is the pyramid height, A the basal area, and D the diameter of the particle. The volume occupied by spheres is

$$V_s = 0.027\pi D^3. \tag{12}$$

The volume of solid spheres occupies 71% of the volume of the pyramid. After the compression, it is assumed that the porous material can be condensed to 100% of its theoretical density. The height of the pyramid will decrease to h'

$$1/3h'A = 0.027\pi D^3 \tag{13}$$

$$h' = 0.58D. \tag{14}$$

The displacement after compression is

$$\Delta h = h - h' = 0.24D. \tag{15}$$

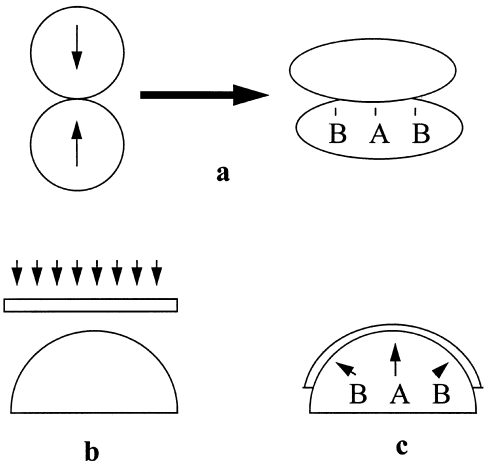

Fig. 9. Large-scale experiment used to simulate particle-to-particle impact in shock consolidation of powders: (a) idealized configuration of two particles prior to and after passage of shock wave; (b) experimental configuration in which plate is accelerated on lateral surface of cylinder; (c) configuration after impact.

The displacement has two components: one is perpendicular to the transmitted force to contact areas and the other is parallel to that.

The perpendicular displacement is

$$d_\perp = \Delta h/2 \cos 60^\circ = 0.06D. \tag{16}$$

Thus the specific friction energy (per unit volume) is

$$E_f = f\mu d_\perp = 0.06f\mu D \tag{17}$$

$$f = \frac{\sqrt{3}P\xi Z}{\rho D}. \tag{18}$$

Thus

$$E_f = \frac{0.1P\xi Z\mu}{\rho} \tag{19}$$

where f is the applied force transmitted to contact areas, μ the friction coefficient, P the applied stress, ρ the density, ξ a fraction of the contact surface, D the particle size, and Z the coordination number of particles.

3.6. Computation of the total energy

The following problem is posed: what pressure is required to shock consolidate a specific material, if interparticle melting with a prescribed thickness is needed for good bonding between particles? It is accepted by the community that metals require an interparticle melt layer in shock consolidation. For ceramics, there is no consensus on the need for this. The results of the present investigation on SiC and diamond indicate that such a layer was present. SiC shows an amorphous layer [18], and diamond exhibits a microcrystalline region [26]. Ahrens *et al.* [27]

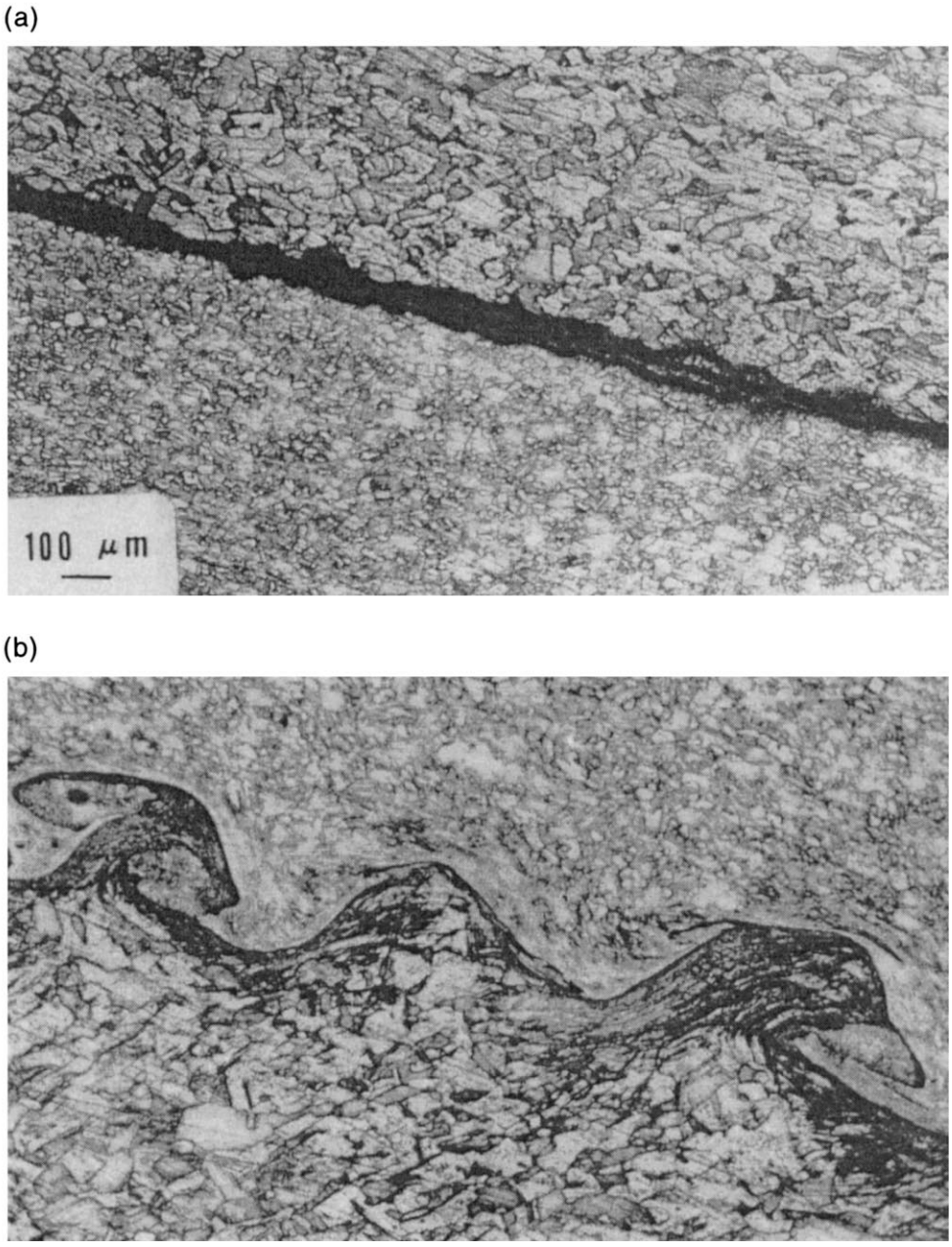

Fig. 10. Appearance of interface in model experiment of Fig. 9: (a) central region which underwent normal impact; (b) lateral region.

performed transmission electron microscopy on shock-consolidated diamond and found evidence for interparticle melting.

The shock wave deposits energy which is associated with the void collapse, microkinetic energy and frictional energy, leading to melting at the powder surfaces, defects (point, line, and interfacial), fractured particles (for brittle materials) and energy release (Fig. 1). Therefore, the specific (per unit volume) total shock energy can be equated as a sum of the specific (per unit volume) void collapse, microkinetic, and frictional energy, leading to

$$E_T = E_{vc} + E_k + E_f = E_d + E_t. \tag{20}$$

This energy, in turn, is equal to the sum of the thermal energy, E_t, and the defect energy, E_d.

The defect energy (which is found to be negligible) is a component of the plastic deformation energy. The Rankine–Hugoniot equations for con-

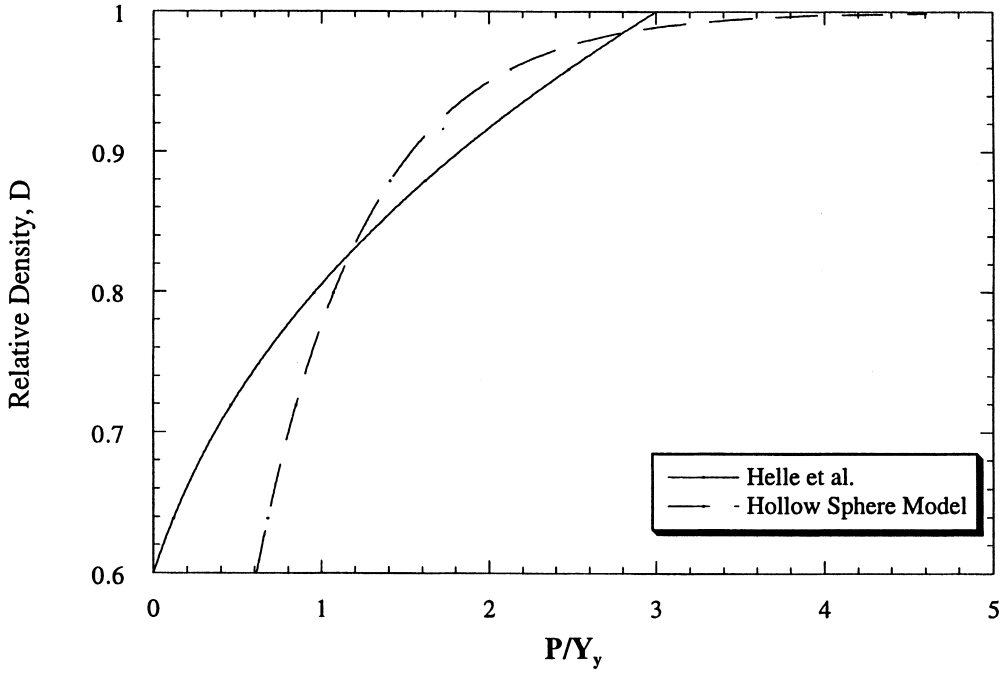

Fig. 11. Pressure as a function of relative density for Helle *et al.* [20] and Hollow Sphere (Carroll–Holt) [24] models.

servation of energy in strong shock conditions:

$$E_s = \frac{P}{2}\left(\frac{1}{\rho_0} - \frac{1}{\rho}\right). \tag{21}$$

Setting $E_T = E_s$ and substituting equations (4), (6) and (8), we obtain

$$P = \frac{2\rho_0\rho}{(\rho - \rho_0)}\left[\frac{1}{2}m\left(\frac{a_0 - c}{\tau}\right)^2 + \frac{0.1P\xi Z\mu}{\rho} + \frac{2.97Y_y}{1-\rho_0}\left(\rho\rho_0 - \frac{(\rho^2 + \rho_0^2)}{2}\right)\right]. \tag{22}$$

The melting energy is a direct result of the plastic deformation, microkinetic, and friction energies. Assuming that the contribution of the plastic energy into the melting energy is negligible, we have

$$E_m = E_k + E_f = \frac{1}{2}m\left(\frac{a_0 - c}{\tau}\right)^2 + \frac{0.1P\xi Z\mu}{\rho}. \tag{23}$$

The above-mentioned assumption concerning the negligible contribution of the plastic energy into the melting energy is indirectly confirmed by the experimental data represented in Fig. 14. It is shown that there exists a linear relationship between the press-

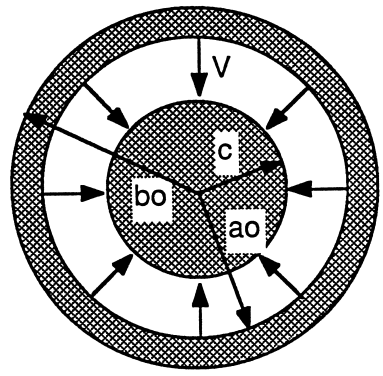

Fig. 12. Carroll–Holt [24] sphere collapse configuration modified by Nesterenko [5] to incorporate micromechanical energy and particle size.

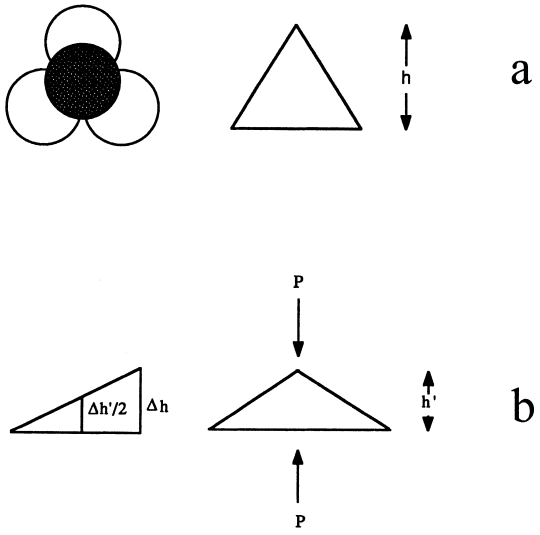

Fig. 13. Pyramidal model used to calculate the frictional energy: (a) prior to compression (height h); (b) after compression (height h').

ure required for shock consolidation and the yield strength of the starting material. This indicates that the strength of the material has a significant influence in the consolidation process. This, in turn, allows the assumption of the consequent action of the void collapse and melting energy dissipation mechanisms. Indeed, if void collapse occurs after the melting of interparticle layers, the consolidation should not be significantly affected by the strength properties of the starting material, in contrast to the data represented in Fig. 14. Thus, one can conclude that melting takes place after a substantial part of void collapse occurs.

We shall prescribe a fixed layer, t, of molten material. The energy required to produce this melting is given by Ferreira and Meyers' modification [6] of the Schwarz *et al.* equation [3] [see also equation (9)]:

$$E_m = \left[\bar{C}_p\left(T_m - T_0 - \frac{E_{vc}}{\bar{C}_p}\right) + H_m\right] \times \left[1 - \left(\frac{D-2t}{D}\right)^3\right]. \tag{24}$$

The term $E_{vc}/\bar{C}_p$ was added to take into account an assumed temperature rise produced by the uniform void collapse process.

Substituting equation (23) into equation (22), taking into account equation (24), we obtain

$$\frac{P}{Y_y} = \frac{2\rho_0\rho}{(\rho-\rho_0)}\left\{\frac{1}{Y_y}\left[\bar{C}_p\left(T_m - T_0 - \frac{1}{\bar{C}_p}\frac{2.97}{1-\rho_0} \times \left(\rho\rho_0 - \frac{(\rho^2+\rho_0^2)}{2}\right)\right) + H_m\right] \times \left[1 - \left(\frac{D-2t}{D}\right)^3\right] + \left(\frac{D-2t}{D}\right)^3 \times \frac{2.97}{1-\rho_0}\left(\rho\rho_0 - \frac{(\rho^2+\rho_0^2)}{2}\right)\right\}. \tag{25}$$

The required thickness t for ceramics and metals can be safely assumed to be in the range 0.1–0.5 and 1–2 μm, respectively. Therefore, the pressure could be estimated directly from equation (25). Notice that the thermal energy generation by friction and microkinetic conversion energy is assumed to be adiabatic, i.e. energy is deposited at the surface layer and a melting layer is formed with no heat transmission to the interior of the particles. The shock pressures required for shock consolidation of Inconel 718, and SiC were calculated. Normalized plots of P/Y_y vs distention ($\alpha = 1/\rho$) were produced for different particle sizes (D). Although no direct experimental verification of this formalism has been obtained until the present (this would require systematic experiments) there is good qualitative agreement. Figure 15 shows these results. As the distention increases, the P/Y_y ratio

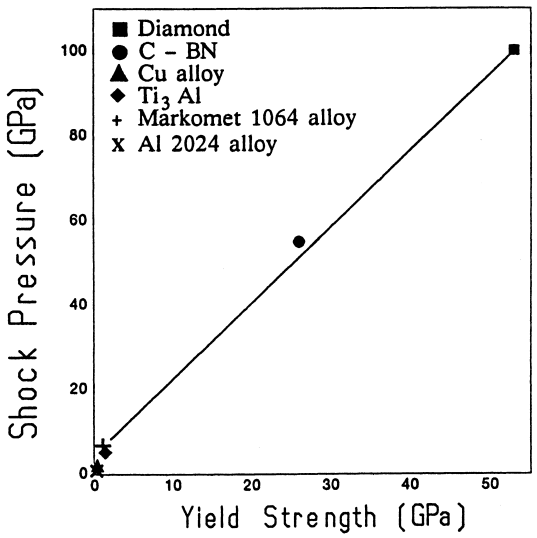

Fig. 14. Correlation between yield strength and pressure required for shock consolidation.

required for shock consolidation of a fixed particle size decreases. Conversely, as the particle size is decreased, the P/Y_y ratio required increases. The shock pressure varies from Y_y to $2Y_y$ for particle sizes in the 20–65 μm range, for the two materials

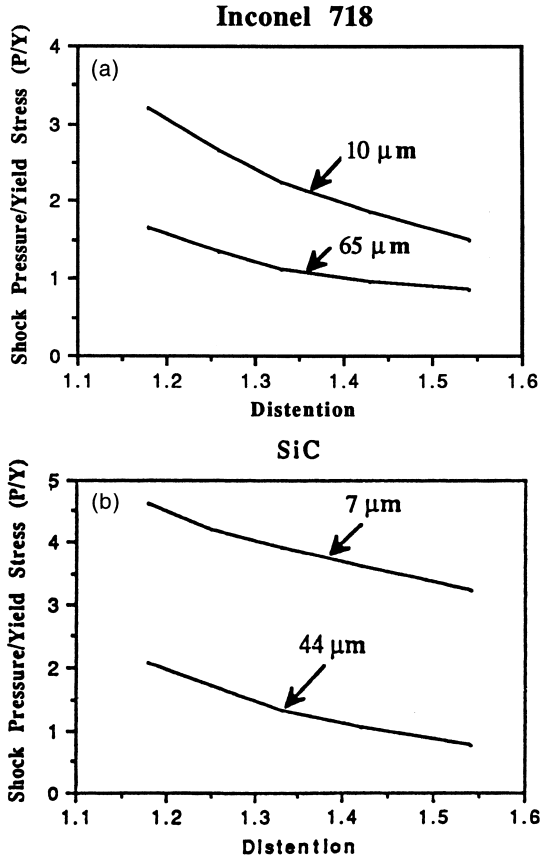

Fig. 15. Shock pressure/yield stress vs distention for (a) Inconel 718 and (b) SiC at different particle sizes.

in Fig. 15, that have widely different thermodynamic and mechanical properties. As the particle size is decreased to 7–15 μm, the pressure required for consolidation increases to the $2Y_y$–$4.5Y_y$ range. These predictions are in full agreement with the experimental results presented in Fig. 14. In these experiments, $D \sim 10$–60 μm. The pressure required for shock consolidation varied between $2Y_y$ and $4Y_y$. In contrast with the models proposed by Schwarz *et al.* [3] and Gourdin [2] the model proposed herein incorporates, prominently, the strength factor. Thus, the energy for shock consolidating a material increases with its strength, all other factors remaining constant.

4. DIRECT NUMERICAL SIMULATION OF SHOCK COMPACTION

The complex deformation pattern occurring in shock consolidation is best captured by computational modeling. The simplifying assumptions in the simple analytical model presented in the previous section are very drastic and the physical processes are only brought out by numerical methods. An accurate and detailed representation of the pressure and the temperature variations during shock consolidation necessitates computational codes. This is done in this section.

The objective of this section is to provide an introduction to multimaterial Eulerian computational methods used in the current research. While there are no textbooks currently available, the review paper by Benson [28] provides additional details on the methods.

The finite element mesh in a Lagrangian formulation deforms with the material, while the mesh in a Eulerian formulation is fixed in space, and the material flows through the Eulerian mesh. Each finite element contains a single material in the Lagrangian formulation, and therefore the elements must follow the material boundaries of the structures. The generation of a mesh that follows the material boundaries is often very difficult for problems with the complicated topologies in experimentally acquired microstructures. In contrast, most Eulerian programs use "logically regular meshes" to simplify their data structures and to optimize their accuracy. Since the Eulerian elements do not follow the material boundaries, they may contain several materials and their contents are described by the volume fractions of their constituent materials.

There are two desirable properties that a transport algorithm should have for an accurate, robust Eulerian formulation:

1. The algorithm should be conservative so that the basic conservation relations for mass, momentum, and energy are satisfied.
2. Second order accuracy is a practical necessity.

One of the most popular methods used in multimaterial Eulerian hydrocodes, and which is used here, is the MUSCL algorithm developed by Van Leer [29]. Greater details of the computational procedure are provided by Benson *et al.* [30].

A model boundary value problem was used to simulate the propagation of the shock wave through the powder. The tridimensional problem is reduced to two dimensions, and spherical particles (of varying diameters) are simulated as cylinders. The green density was taken as 80% of the theoretical density, and calculations were performed for copper and silicon carbide. The Steinberg–Guinan plasticity model [31] was used in combination with the Mie–Gruneisen equation of state. A particle size distribution was assumed based on experimental measurements.

Figure 16 shows the original configuration of the powders, whereas the configurations after shock impact velocities of 0.25, 1, and 2 km/s on Inconel 718 powders are shown in Fig. 17. At 0.25 km/s, the shock energy is sufficient to collapse all voids. As the impact velocity is increased, the "microkinetic" energy of the powders increases, and plastic deformation at the interfaces significantly exceeds the value needed for void collapse. A detailed analysis of computationally-obtained microkinetic energy was recently published by Benson *et al.* [30]. Thus, one can separate this plastic deformation into a "geometrically necessary" component and a "redundant" component; the latter is due to the microkinetic energy and is responsible for the localized temperature spikes that lead to melting and bonding. At 2 km/s, the Inconel 718 powder is severely deformed with a great amount of "redundant" plastic deformation due to the microkinetic energy. Figure 18 shows the results of the computation for SiC powder at impact velocities of 0.5, 1, and 1.5 km/s, respectively. At 2 km/s, the shock

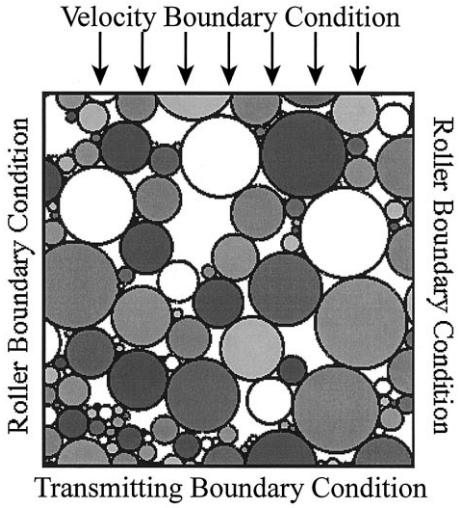

Fig. 16. The model boundary value problem for cylindrical particles with an initial porosity of 19%.

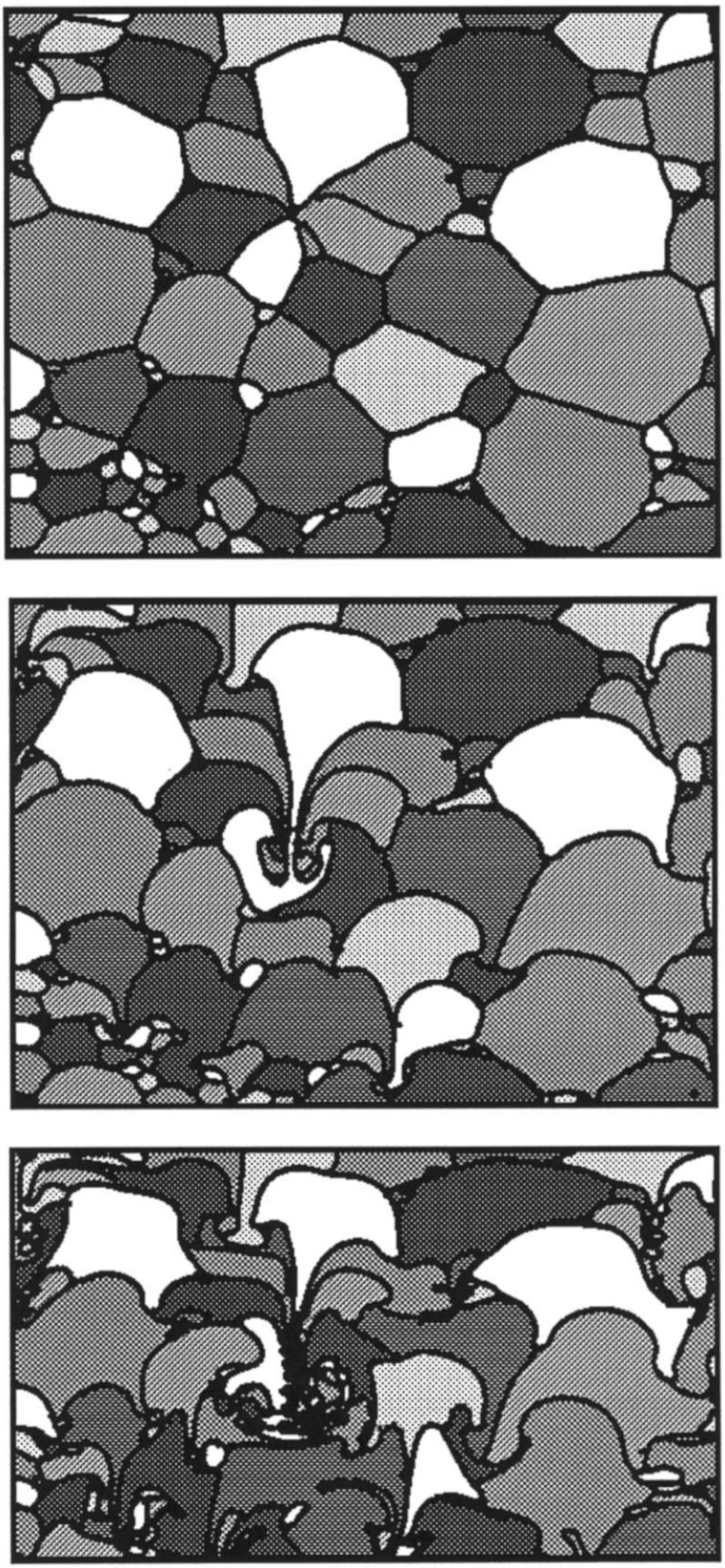

Fig. 17. The final configurations for the cylindrical particles of Inconel 718 with an initial porosity of 19% and particle velocities of 0.25, 1.00, and 2.00 km/s.

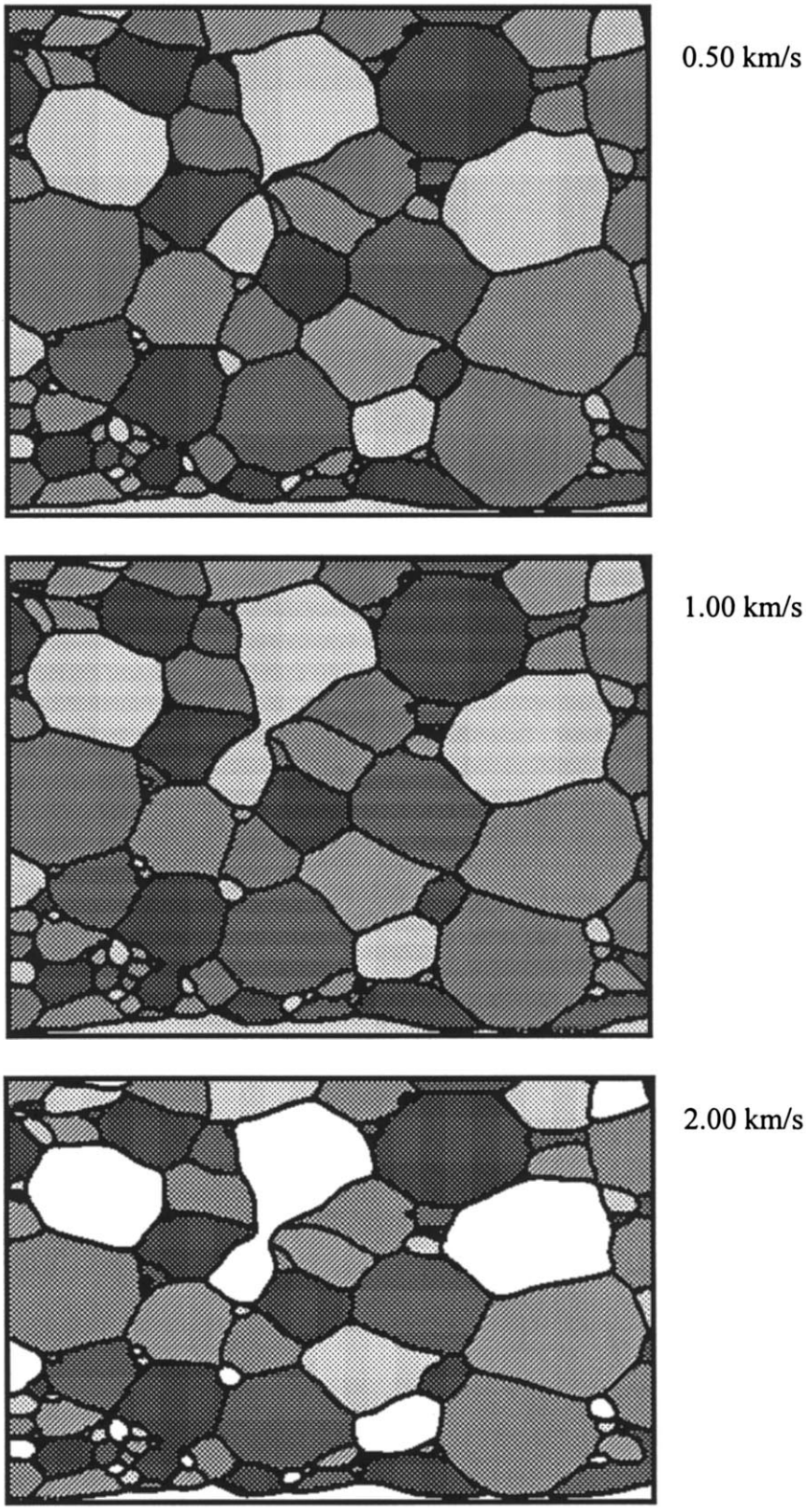

Fig. 18. The final configurations of SiC with an initial porosity of 19% and particle velocities of 0.5, 1.00, and 2.00 km/s.

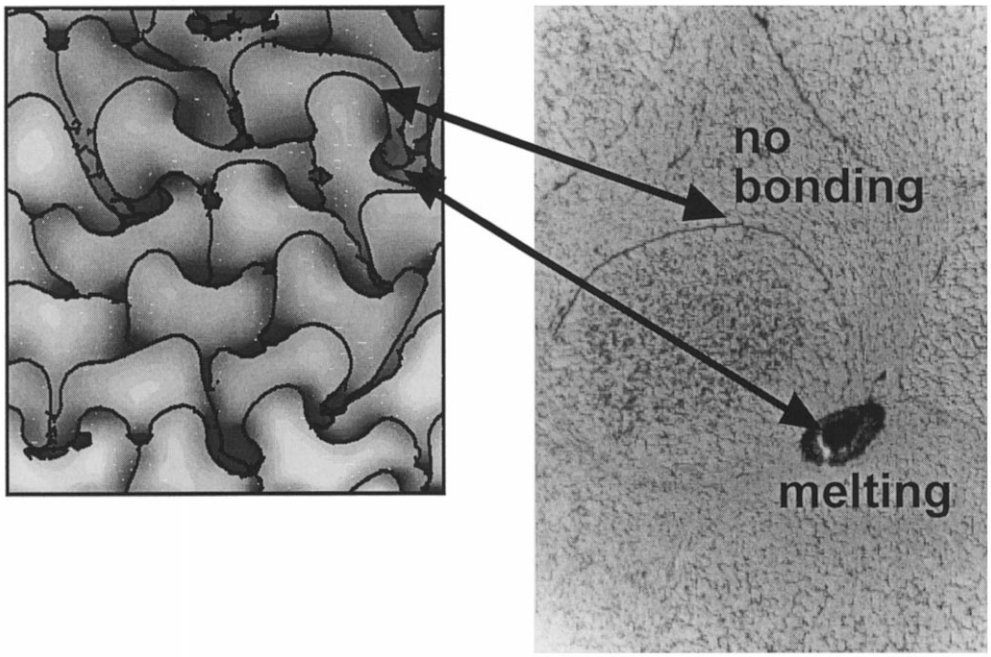

Fig. 19. Temperature distributions in shock-consolidated Inconel 718.

energy is only sufficient to collapse the voids in SiC. This explains why the shock pressure required for consolidation of SiC is much higher than for Inconel 718. These predictions are confirmed by shock compaction experiments carried out by Kondo *et al.* [10]. The formation of "hot spots" leading to interparticle melting only occurs at much higher pressures. The relative temperature distribution in shock-consolidated Inconel 718 is represented in Fig. 19. The highest temperature, and therefore, the probability of melting (and bonding) is observed at particle corners.

5. LIMITATIONS OF SHOCK CONSOLIDATION PROCESS

As discussed in Section 2, there exist two major problems in shock consolidation. One is cracking of the compacts at both the microscopic and macroscopic levels. The other is a lack of uniformity in microstructure and mechanical properties within the resulting compacts. As the shock wave propagates through the powders, it generates tensile stresses. These tensile stresses, at the particle level, are accommodated by plastic deformation in ductile materials; in brittle materials, cracks are generated within the particles by the activation of existing flaws. An assessment of the stresses generated by the propagation of shock waves through particles is given in Section 5.1. A second factor, of great importance, is the tension generated within the consolidated specimen by reflected tensile waves.

These stresses are discussed in Section 5.2.

5.1. Tension in particles by propagation of shock waves

A simple model is presented below to represent a cylindrical particle subjected to a compression, along the center of its top surface, by the shock wave entering it and being supported at the bottom by two particles. Figure 20 shows the configuration of equisized particles used for the computation carried out by finite elements. The pressure applied to the surrounding particles, shown in Fig. 20 was taken equal to 10 GPa. This is in the range of pressures required for shock consolidation of ceramics. The region of the particle subjected to tension is marked, and tensile stresses vary from 0 to 6 GPa. The pressure of these high tensile stresses in concomitance with flaws existing in the ceramics can lead to failure by tensile crack propagation, yielding a microstructure typified by Fig. 7. The fracture toughness of SiC is typically 5–10 $MN/m^{3/2}$, and the size of flaws that can be activated, at this maximum stress level, is

$$a = \frac{K_{Ic}^2}{\pi\sigma^2} = 0.65\ \mu\text{m}. \tag{26}$$

Thus, if flaws are present in the hatched area of Fig. 20, they can be activated by the tensile stresses. It is clear from the above that particle sizes in the sub-micron range are required if particle fracturing during shock-wave propagation is to be avoided. This yields an impetus for implementation of shock-compaction technologies for pressure treatment of ultrafine powders [32, 33].

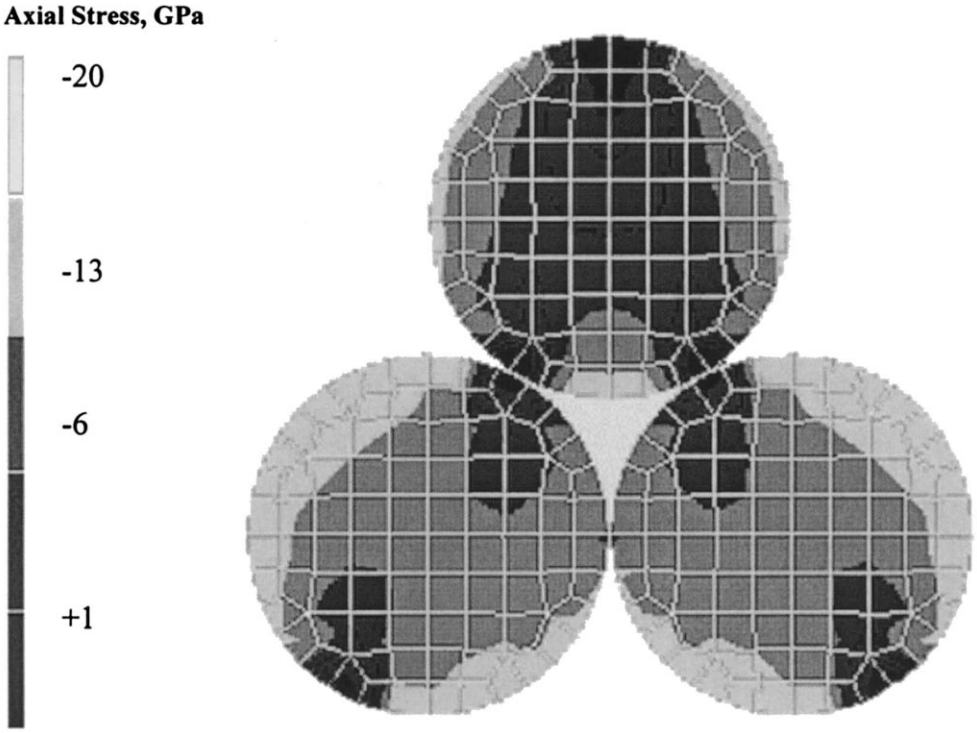

Fig. 20. Isostress bands computed for normal stress perpendicular to the (vertical) direction of loading; positive stresses are tensile and negative stresses are compressive.

5.2. Tension produced by reflected waves

Figure 21(a) shows plots of critical size, a, as a function of tensile stress σ for materials having different fracture toughnesses, K_{1c}. These plots were made using the well-known fracture mechanics equation: $\sigma = K_{1c}/\sqrt{(\pi a)}$. It is difficult to conceive a shock consolidation process in which no flaws are left, and the particle size is a good indicator of the inherent flaw size in a shock consolidated material. The three fracture toughnesses given, 5, 50, and 100 MPa $m^{1/2}$, are characteristic of brittle (ceramics), tough (steel, titanium alloys), and very ductile materials (copper, nickel), respectively. Figure 21(b) shows the critical tensile stresses for 25 and 10 μm particle sizes as a function of the compressive stresses needed to consolidate the respective powders. The compressive stresses were taken from Ferreira and Meyers' calculation [6], at a distention corresponding to an initial density of 65% of the theoretical density (this is a typical value for powders). Tensile stresses due to reflections are always present in shock consolidation systems. Tensile stresses due to reflections are residual stresses due to the loading inhomogeneity and the temperature gradient of cooling. The amplitude of the reflected tensile stresses can be as high as the compressive stresses. However, in well-designed systems a significant portion of the tensile stresses is trapped. When the tensile stresses exceed the critical tensile stresses for the specific material, failure occurs; this is shown in Fig. 21(b) in a schematic fashion. A realistic line shows $\sigma_t = 0.1\sigma_c$, i.e. the tensile reflections have, at most, an amplitude of 10% of the compressive pulse. By reducing the shock amplitude, point A (corresponding to a hypothetical material) is changed to B.

5.3. Residual stresses

Shock consolidation generates large thermal gradients because of the very short times over which the entire deformation process takes place. These high thermal gradients produce large residual stresses on cooling. Post-deformation cracking has been observed to occur on heating, due to these high residual stresses. Cracking is also often observed when the capsules containing specimens are removed, and the compressive stresses from them are released.

This is a phenomenon of great importance which imposes a potential limitation on the process.

5.4. Recommended approaches

In spite of the limitations and problems, there are few approaches that can be implemented for improved shock consolidation:

1. Reduction of tensile stresses. Reduction of tensile stresses requires systems where the design geometry is optimized.
2. Reduction of shock energy. Shock energy can be reduced by (a) chemical or (b) thermal energy in an effort to improve compact quality. Chemical energy can be provided by reactive mixtures

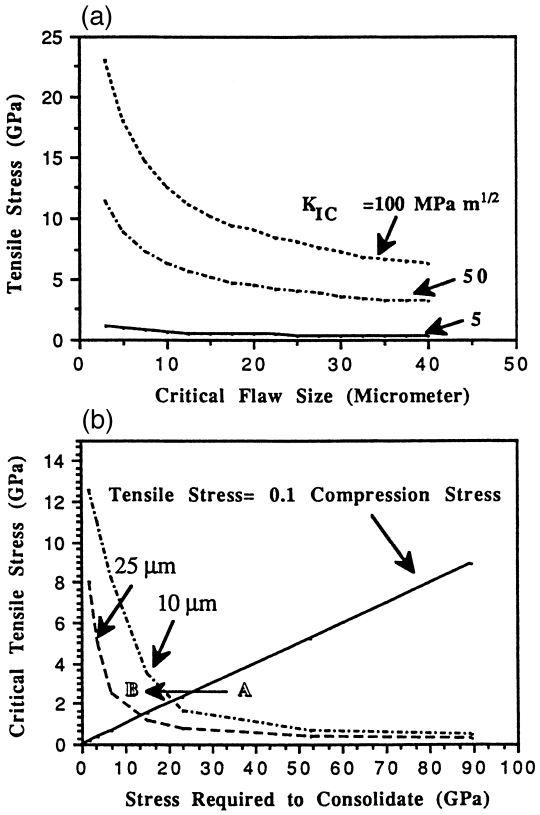

Fig. 21. (a) Critical flaw size as a function of tensile stress for materials with different fracture toughnesses. (b) Variation of critical tensile stress for 0.1, 10, and 25 μm flaw activation with shock stress required for consolidation: notice regions favorable and unfavorable for consolidation.

added to the powders. This has been introduced by Akashi and Sawaoka [17] for ceramics and successfully extended by Yu and Meyers [34] for intermetallics. The energy released by the reaction helps to heat the powders, whereas the reaction products are very hot and provide the "glue". Direct heating can be accomplished by hot shock consolidation; indeed, this method has yielded considerable improvement over room-temperature consolidation for a number of very hard materials [33, 35–37]. The recent results by Hokamoto and co-workers [38–40] are particularly encouraging.

3. Reduction of particle size. The reduction in powder size (e.g. nanocrystalline), reducing a, the flaw size, thereby enables the application of higher tensile stresses without opening cracks. This approach has been successfully implemented by Kondo and co-workers [10, 32, 33].
4. Post-shock heat treatments. Molotkov *et al.* [41], Shang *et al.* [26], Meyers *et al.* [37], Coker *et al.* [42], and Shang and Meyers [43] used HIPing to heal existing flaws and successfully improved the performance of shock compacted powders.
5. Shock densification followed by diffusional bonding (annealing or HIPing). This approach is based on a low-amplitude shock pulse that serves primarily to densify the material. It is followed by a thermal treatment that provides the diffusional bonding between the grains.

6. CONCLUSIONS

Although shock consolidation is a promising method to produce monolithic ceramics, metals, and composites, cracking due to tensile reflected stresses and residual stresses is a major problem. This problem is especially acute with materials with a high hardness. While it is relatively easy to consolidate soft metals such as copper, aluminum and iron, the consolidation of flaw-free ceramics has not been accomplished yet. An analysis was performed of shock energy dissipation by the porous medium. The analysis extends the concepts advanced by Gourdin [2], Schwarz *et al.* [3], Nesterenko [5], and Ferreira and Meyers [6]. The most important energy dissipation processes were identified:

1. Plastic deformation energy, E_{vc}: this represents the energy expended in collapsing the voids between the particles.
2. Microkinetic energy, E_k: the material acquires kinetic energy as it moves into the voids.
3. Frictional energy, E_f: particles reorganize themselves during shock compaction, with friction between neighbors.

Melting is a direct result of plastic deformation, microkinetic, and frictional energies. Quantitative expressions were developed for these three energy dissipation processes. The conservation-of-energy equation was used in combination with a prescribed interparticle melt layer in order to obtain shock amplitude predictions for consolidation of different materials. The results lead to predictive guidelines for the design of compaction systems. These expressions, as well as hydrodynamic calculations, predict energies required for the shock consolidation of powders with different mechanical properties. These energies are of such magnitude that, for harder materials, flaws are activated by the reflected waves, which break up the compacts. Thus, shock consolidation of powders might be a conundrum that escapes any straightforward solution.

Acknowledgements—The explosive experiments were carried out at New Mexico Tech., Socorro, New Mexico through the kind assistance of N. N. Thadhani. Discussions with V. F. Nesterenko and A. Sawaoka are gratefully acknowledged. The help provided by S. S. Shang, A. Ferreira, S. L. Wang, and A. Szecket was essential to the success of this work. The research was partly supported by the National Science Foundation Institute for Mechanics and Materials and by the U.S. Army Research Office Multidisciplinary Research Initiative (MURI) through Contract No. DAAH04-91-10376.

REFERENCES

1. Prummer, R., *Explosivverdichtung Pulveriger Substanzen*. Springer, Berlin, 1987.
2. Gourdin, W. H., *J. appl. Phys*., 1984, **55**, 172.
3. Schwarz, R. B., Kasiraj, P., Vreeland, T. Jr and Ahrens, T. J., *Acta metall*., 1984, **32**, 1243.
4. Raybould, D., Morris, D. G. and Cooper, G. A., *J. Mater. Sci*., 1979, **14**, 2523.
5. Nesterenko, V. F., in *Metallurgical and Materials Applications of Shock-Wave and High-Strain-Rate Phenomena*, ed. L. E. Murr, K. P. Staudhammer and M. A. Meyers. Elsevier, Amsterdam, 1995, p. 3.
6. Ferreira, A. and Meyers, M. A., in *Shock Wave and High Strain Rate Phenomena in Materials*, ed. M. A. Meyers, L. E. Murr and K. P. Staudhammer. Marcel Dekker, New York, 1992, p. 361.
7. Ahrens, T. J., Bond, G. M., Yang, W. and Lin, G., in *Shock Waves and High Strain Rate Phenomena in Materials*, ed. M. A. Meyers, L. E. Murr and K. P. Staudhammer. Marcel Dekker, New York, 1992, p. 339.
8. Sawaoka, A. B. (ed.), *Shock Waves in Materials Science*. Springer, Tokyo, 1992.
9. Horie, Y. and Sawaoka, A. B., *Shock Compression Chemistry of Materials*. K. T. K. Science, Tokyo, 1993.
10. Kondo, K. I., Soga, S., Sawaoka, A. and Araki, M., *J. Mater. Sci*., 1985, **20**, 1033.
11. Matsumoto, H. and Kondo, K.-I., *J. Mater. Sci*., 1989, **24**, 4042.
12. Benson, D. J. and Nellis, W. J., in *High Pressure Science and Technology*, ed. S. C. Schmidt, J. W. Shaner, G. A. Samara and M. Ross. American Inst. of Phys. Press, NY, 1993, p. 1243.
13. Williamson, R. L., *J. appl. Phys*., 1990, **68**, 1287.
14. Meyers, M. A. and Murr, L. E., in *Shock Waves and High Strain Rate Phenomena in Metals*, ed. M. A. Meyers and L. E. Murr. Plenum Press, New York, 1981, p. 487.
15. Lotrich, V. F., Akashi, T. and Sawaoka, A. B., in *Metallurgical Applications of Shock Waves and High-Strain-Rate Phenomena*, ed. L. E. Murr, K. P. Staudhammer and M. A. Meyers. Marcel Dekker, New York, 1986, p. 277.
16. Elliott, X. X. and Staudhammer, K. P., in *Shock Waves and High Strain Rate Phenomena in Materials*, ed. M. A. Meyers, L. E. Murr and K. P. Staudhammer. Marcel Dekker, New York, 1992, p. 371.
17. Akashi, T. and Sawaoka, A. B., U.S. Patent 4.655.830, 1987.
18. Shang, S. S. and Meyers, M. A., *J. Mater. Sci*., 1996, **31**, 252.
19. Wang, S. L., Meyers, M. A. and Szecket, A., *J. Mater. Sci*., 1988, **23**, 1786.
20. Helle, A. S., Easterling, K. E. and Ashby, M. F., *Acta metall*., 1985, **33**, 2163.
21. Olevsky, E. A., *Mater. Sci. Engng R: Reports*, 1998, **23**, 40.
22. Hill, R., *The Mathematical Theory of Plasticity*. Oxford University Press, Oxford, 1950.
23. Fischmeister, H. F. and Arzt, E., *Powder Metall*., 1983, **26**, 82.
24. Carroll, M. M. and Holt, A. C., *J. appl. Phys*., 1972, **43**, 1626.
25. Meyers, M. A. and Chawla, K. K., *Mechanical Metallurgy*. Prentice-Hall, Englewood Cliffs, New Jersey, 1984, p. 241.
26. Shang, S. S., Hokamoto, H. and Meyers, M. A., *J. Mater. Sci*., 1992, **27**, 5470.
27. Ahrens, T. J., Bond, G. M., Yang, W. and Liu, G., in *Shock Waves and High Strain Rate Phenomena in Materials*, ed. M. A. Meyers, L. E. Murr and K. P. Staudhammer. Marcel Dekker, New York, 1992, p. 339.
28. Benson, D. J., *Comp. Meth. Appl. Mech. Engng*, 1992, **99**, 235.
29. Van Leer, B., *J. Comp. Phys*., 1979, **32**, 101.
30. Benson, D. J., Nesterenko, V. F., Jonsdottir, F. and Meyers, M. A., *J. Mech. Phys. Solids*, 1997, **45**, 1955.
31. Steinberg, D. J. and Guinan, M. W., Technical Report UCRL-80465, Lawrence Livermore National Laboratory, 1978.
32. Kondo, K. I. and Sawai, S., *J. Am. Ceram. Soc*., 1990, **73**(7), 1983.
33. Kondo, K. I. and Sawai, S., in *Science and Technology of New Diamond*, ed. S. Saito, O. Fukunaga and M. Yoshikawa. K. T. K. Science, Tokyo, 1990, p. 245.
34. Yu, L. H. and Meyers, M. A., *J. Mater. Sci*., 1991, **26**, 601.
35. Hokamoto, H., Fujita, M., Chiba, A., Itoh, S., Tanaka, S., Hirose, M., Kugimotu, T. and Tomoshige, R., in *Shock Waves and High Strain Rate Phenomena in Materials*, ed. L. E. Murr, K. P. Staudhammer and M. A. Meyers. Elsevier, Amsterdam, 1995, p. 117.
36. Wang, S. L., Meyers, M. A. and Szeket, A., *J. Mater. Sci*., 1988, **23**, 1786.
37. Meyers, M. A., Shang, S. S. and Hokamoto, K., in *Shock Waves in Materials Science*, ed. A. B. Sawaoka. Springer, Tokyo, 1993, pp. 145–176.
38. Hokamoto, K., Fujita, M., Tanaka, S., Kodama, T. and Ujimoto, Y., *Scripta mater*., 1998, **39**, 1383.
39. Tanaka, S., Hokamoto, K., Fujita, M., Itoh, S. and Mashimo, T., *Physica B*, 1997, **239**, 16.
40. Hokamoto, K., Tanaka, S., Fujita, M., Itoh, S., Meyers, M. A. and Chen, H. C., *Physica B*, 1997, **239**, 1.
41. Molotkov, A. V., Notkin, A. B., Elagin, D. V., Nesterenko, V. F. and Lazaridi, A. N., *Combust. Explosions Shock Waves*, 1991, **27**, 377.
42. Coker, H. L., Meyers, M. A. and Wessels, J. F., *J. Mater. Sci*., 1991, **26**, 1277.
43. Shang, S. S. and Meyers, M. A., *Metall. Trans*., 1991, **22A**, 2667.